ACCSCIENCE PUBLISHING

International Journal of Bioprinting

RESEARCH ARTICLE

# Si–C covalent bonding-mediated interfacial charge transfer enhances photodynamic antitumor effects of selective laser sintered bone scaffolds

**Bingxin Sun[1†], Zhiheng Yu[2†], Shuping Peng[3], Weifan Dai[1], Jiaxiang Wu[1], Guoyong Wang[1*], and Cijun Shuai[1,4*]**

[1]Jiangxi Provincial Key Laboratory of Additive Manufacturing of Implantable Medical Device, Jiangxi University of Science and Technology, Nanchang, Jiangxi, China

[2]Department of Mechanical Engineering, College of Mechanical and Electrical Engineering, Jiaxing Nanhu University, Jiaxing, Zhejiang, China

[3]The Key Laboratory of Carcinogenesis and Cancer Invasion of the Chinese Ministry of Education of Xiangya Hospital and School of Basic Medical Science, Central South University, Changsha, Hunan, China

[4]State Key Laboratory of Precision Manufacturing for Extreme Service Performance, College of Mechanical and Electrical Engineering, Central South University, Changsha, Hunan, China

(This article belongs to the *Special Issue: 3D Printing in Clinical Application*)

## Abstract

Nitrogen-doped carbon dots (NCDs) show promising potential in photodynamic antitumor applications due to their appropriate band gap and photo-responsiveness. Nevertheless, their therapeutic efficacy is limited by both a low reactive oxygen species (ROS) quantum yield and their propensity for aggregation. Herein, NCDs were encapsulated within mesoporous silica nanoparticles (MSNs) to fabricate an effective photosensitizer (NCDs@MSN) via a one-pot hydrothermal method. The covalent Si–C bonds formed between NCDs and MSNs enhanced interfacial charge transfer, thereby substantially amplifying the generation of ROS under hypoxic conditions. Meanwhile, the mesoporous structure of MSNs prevented NCD aggregation and provided a larger accessible surface area with more exposed active sites. Electron spin resonance spectroscopy confirmed the light-triggered generation of ROS, validating its potent ROS generation capacity under hypoxia. Subsequently, NCDs@MSN were incorporated into poly-L-lactic acid to fabricate a composite scaffold via selective laser sintering, which was designed for postoperative photodynamic management of tumorous bone defects. The resulting scaffold exhibited potent photodynamic cytotoxicity against tumor cells alongside excellent biocompatibility. This work presents a potential strategy for engineering intelligent implants to prevent postoperative tumor recurrence.

***Keywords:*** Nitrogen-doped carbon dots; Photodynamic therapy; Scaffold; Antitumor; Selective laser sintering

*[†]These authors contributed equally to this work.*

***Corresponding authors:**
Cijun Shuai
(shuai@jxust.edu.cn)
Guoyong Wang
(wangguoyong@jxust.edu.cn)

**Citation:** Su B, Yu Z, Peng S, *et al.* Si–C covalent bonding-mediated interfacial charge transfer enhances photodynamic antitumor effects of selective laser sintered bone scaffolds. *Int J Bioprint.* 2026:12(2):026030020.
doi: 10.36922/IJB026030020

**Received:** January 12, 2026

**Revised:** March 2, 2026

**Accepted:** March 3, 2026

**Published online:** April 15, 2026

## 1. Introduction

Osteosarcoma is a highly malignant bone tumor that poses a significant threat to adolescents and young adults.[1] Surgical resection and bone grafting are important strategies for the clinical treatment of osteosarcoma.[2] However, postoperative management remains a significant clinical challenge due to the high propensity for recurrence and metastasis of tumor cells. Therefore, various treatment strategies are being rapidly developed to eradicate residual tumor cells, including chemotherapy, radiotherapy, and photodynamic therapy (PDT). Among them, PDT has become a promising approach for the postoperative management of tumorous bone defects, due to its spatiotemporal precision and favorable safety.[3] The efficacy of PDT is directly linked to the light-activated generation of reactive oxygen species (ROS) by photosensitizers (PSs), propelled by either type I (electron transfer) or type II (energy transfer) mechanisms.[4] Conventional organic PSs predominantly operate through the type II pathway, which is highly oxygen-dependent and involves the production of singlet oxygen ($^1O_2$). However, the hypoxic microenvironment characteristic of osteosarcoma severely limits the PDT efficiency. In contrast, type I PSs mediate electron transfer reactions to generate oxygen-independent free radicals,[5] such as superoxide anions ($\bullet O_2^-$) and hydroxyl radicals (•OH), offering a compelling alternative for overcoming hypoxia-mediated resistance.[6]

Recently, various type I PSs have been developed and applied for photodynamic antitumor therapy in hypoxic environments, such as metal–organic frameworks, metal oxides/sulfides, and nitrogen-doped carbon dots (NCDs). Particularly, NCDs exhibit both photosensitivity and peroxidase (POD) activity,[7] enabling them to catalyze redox reactions with endogenous $H_2O_2$ within tumor cells and generate ROS such as •OH and $\bullet O_2^-$.[8] However, the rapid recombination of photogenerated electron-hole pairs, resulting from the short excited-state lifetime of NCDs, significantly limits their efficiency in PDT applications. Additionally, the aggregation of NCDs caused by surface polar groups and van der Waals interactions reduces light absorption ability and photocatalytic efficiency, further compromising ROS production. To address these issues, several engineering strategies have been explored to promote the tumor-specific accumulation and stability of NCDs. For example, surface modification with polyethylene glycol enhances the water solubility and circulation time of carbon dots, as demonstrated by Peng *et al.*[9] However, excessively long polyethylene glycol chains can attenuate cellular interactions. Zhang *et al.* synthesized Fe-CDs via a metal ion doping approach, improving the catalytic and electron transport properties of carbon dots,[10] but potential ion leaching may induce oxidative stress or hamper biosafety.

The rational design of nanoscale support matrices for anchoring NCDs not only suppresses electron-hole recombination and exposes abundant active sites but also effectively prevents the aggregation of NCDs. Mesoporous silica nanoparticles (MSNs) represent an ideal platform for constructing such nanocarriers, owing to their tunable pore sizes (2–50 nm), large specific surface areas (up to >1000 $m^2/g$), and facile surface functionalization.[11] Particularly, the robust tetrahedral siloxane framework has high stability, enabling effective encapsulation of nanomaterials.[12] Building on this foundation, we propose to anchor NCDs onto MSN and hypothesize that covalent Si–C bonds can form at the NCD–MSN interface, which would facilitate interfacial charge transfer. Furthermore, the ordered mesoporous structure would provide spatial confinement that not only inhibits the aggregation of NCDs but also enhances interactions with substrates. Collectively, these synergistic features are expected to amplify ROS generation capacity of the NCDs, thereby offering a promising strategy to improve the efficacy of PDT.

Considering that the rapid recombination of photogenerated electrons and holes in NCDs severely limits the generation efficiency of ROS, enhancing the charge separation and transfer capability of the materials has become crucial for achieving highly efficient photocatalytic performance. The unique mesoporous structure of MSN effectively promotes interfacial charge transfer and simultaneously inhibits the aggregation of NCDs through spatial confinement, thereby synergistically enhancing their catalytic activity. In recent years, scaffold-based tumor therapeutic systems have become a research hotspot. For instance, Lee *et al.*[13] developed a 3D-printed magnesium-doped hydroxyapatite nanoneedle polylactic acid scaffold, which successfully integrated photothermal antitumor activity with vascularized bone regeneration. Inspired by this design concept of inorganic-doped scaffolds, the present study employed a one-pot hydrothermal method to construct a type I photosensitizer (NCDs@MSN), which was subsequently compounded with poly-L-lactic acid (PLLA). A photodynamic antitumor scaffold was then fabricated using selective laser sintering (SLS). The charge transfer kinetics of NCDs@MSN were systematically evaluated through transient photocurrent response and electrochemical impedance spectroscopy. Combined with probe degradation and spin-trapped electron paramagnetic resonance techniques, the scaffold's ROS generation capability and POD-like activity under 640 nm light excitation were quantitatively analyzed.

In vitro biological experiments further confirmed the scaffold's high efficacy in killing tumor cells, and its biocompatibility was comprehensively assessed via cell adhesion observation, fluorescence staining, and Cell Counting Kit-8 (CCK-8) proliferation assays.

## 2. Materials and methods

### 2.1. Materials

Poly-L-lactic acid was obtained from Shenzhen Boli Biomaterials Co., Ltd (China). Cetyltrimethylammonium chloride (CTAC), triethanolamine (TEA), citric acid (CA), and ethylenediamine (EDA) were purchased from Shanghai Aladdin Biochemical Technology Co., Ltd (China). Tetraethyl orthosilicate (TEOS) was purchased from Shanghai Rhawn Reagent Co., Ltd (China).

### 2.2. Synthesis of NCDs@MSN and NCDs/MSN

According to the previously reported synthesis method,[14] 0.6 g of CTAC and 0.12 g of TEA were added to 40 mL of deionized water and stirred until fully dissolved. The solution was then placed at 95 °C and stirred for 60 min, after which 3.0 g of TEOS was added dropwise into the system. Once the TEOS addition was complete, 2.0 g of CA and 0.6 mL of EDA were added sequentially, and the mixture was further stirred at 95 °C for 60 min. Finally, the mixed solution was transferred into a Teflon-lined autoclave and hydrothermally treated at 150 °C for 2 h. Then, the product underwent ultrasonic treatment in hydrochloric acid/ethanol solution (volume ratio 1:9) for 1 h to remove the template. A white powder was obtained after freeze-drying. NCDs were synthesized using the same method, with only CA and Ethylenediamine

(EAN) employed as precursors. NCDs/MSN composites were prepared by dispersing 0.4 g of mesoporous silica in 30 mL of ethanol, followed by the addition of 5% NCDs. The mixture was stirred at room temperature for 8 h, then centrifuged and freeze-dried to yield the final product.[15]

### 2.3. Fabrication of scaffolds

Poly-L-lactic acid was blended with NCDs, NCDs@MSN, and NCDs/MSN, then added to absolute ethanol to form the PLLA/NCDs, PLLA/NCDs@MSN, and PLLA/NCDs/MSN mixtures, respectively. After mixing by magnetic stirring and ultrasonic dispersion, the resulting product was dried and ground to obtain composite powders. The scaffolds (diameter: 5 mm, thickness: 3 mm) were fabricated by SLS (YB-24Y-30, Yiben Optoelectronics Co., Ltd. China).[16] Laser sintering parameters used are as follows: layer thickness 0.1 mm, laser scanning speed 180 mm/s, and laser power 3.5 W.

### 2.4. Nanoparticle characterization

The morphology and crystal structure of the nanoparticles were characterized using transmission electron microscopy (TEM; JEOL JEM-F200, JEOL Ltd., Japan), while their element distribution and composition were analyzed using energy dispersive spectroscopy (EDS; JEOL JEM-F200, JEOL Ltd., Japan). The phase composition and crystal structure of the nanoparticles were examined with an X-ray diffractometer (D8 Advance, Bruker, Germany). The elemental composition and chemical valence states of the material were probed by an X-ray photoelectron spectrometer (XPS; K-Alpha, Thermo Scientific, United States of America [USA]).

### 2.5. Characterization of scaffolds

The surface morphology and elemental composition of the scaffolds were characterized by scanning electron microscopy (SEM; EVO18, ZEISS, Germany). The mechanical properties of the scaffolds were evaluated using a universal testing machine (E44.304, Mattes Industrial Systems Co., LTD, China). For tensile testing, dumbbell-shaped specimens (13 × 5 × 2 mm) were prepared, while porous cuboid samples (3 × 4 × 5 mm) were used for compressive testing, following established protocols.[17]

### 2.6. Fluorescence measurement

NCDs and NCDs@MSN powders were dispersed in deionized water, sonicated for 10–15 min to form homogeneous suspensions, and then transferred to quartz cuvettes with a final volume of 3 mL. Fluorescence spectra were acquired using a spectrofluorometer. Photoluminescence (PL) spectra were recorded by scanning the emission range with optimized excitation wavelengths for each sample. Subsequently, without repositioning the cuvettes, PL excitation spectra were measured by scanning the excitation range at fixed emission wavelengths corresponding to the respective PL maxima. Additionally, emission spectra of NCDs@MSN were collected under various excitation wavelengths to investigate their excitation-dependent fluorescence behavior.

### 2.7. Electrochemical measurement

Electrochemical measurements were performed using a three-electrode system with a nanoparticle-coated conductive glass as the working electrode, an Ag/AgCl electrode as the reference electrode, and a platinum plate as the counter electrode. To ensure that the experiments accurately reflected the material's behavior in a humid physiological environment, the three-electrode setup was immersed in an aqueous electrolyte solution of 0.5 mol/L $Na_2SO_4$ this concentration of $Na_2SO_4$ was chosen to

provide sufficient ionic conductivity, mimicking the ionic strength of biological fluids, while remaining relatively inert and allowing for the clear observation of the intrinsic electrochemical properties of the bare NCDs and the NCDs@MSN composite. The electrolyte volume of 50 mL ensured complete electrode immersion and stable test conditions. By utilizing different test modules within the workstation software, the time-dependent photocurrent curves, impedance curves, and Mott-Schottky curves of both NCDs and NCDs@MSN were determined.

### 2.8. Reactive oxygen species generation of the scaffolds

To measure $\bullet O_2^-$ generation, nitroblue tetrazolium (NBT) was used as the capture agent for $\bullet O_2^-$. The tested scaffolds were separately placed in reaction systems containing 3 mL of NBT solution, and reacted at room temperature for 30 min under 640 nm LED irradiation (100 mW $cm^{-2}$). The use of an aqueous NBT solution directly interfaces the materials with a reactive probe in a liquid medium, mimicking the presence of biological fluids. The supernatant was collected after the reaction, and its absorbance at 560 nm was measured using a UV-visible spectrophotometer. This wavelength corresponded to the characteristic absorption peak of formazan generated by the reaction between NBT and $\bullet O_2^-$.

The amount of $\bullet O_2^-$ generated was evaluated by the change in absorbance (the absorbance increases with the concentration of $\bullet O_2^-$). For the detection of $\bullet O_2^-$ under hypoxic conditions, a similar method was employed, except that the mixed solution was purged with $N_2$ for 30 min prior to irradiation with a 640 nm LED light.

Hydroxyl radical generation was evaluated using the methylene blue (MB) colorimetric method. The tested scaffold samples were separately placed in reaction systems containing 3 mL of MB solution. The reaction was conducted at room temperature for 30 min under 640 nm LED irradiation (100 mW $cm^{-2}$). This aqueous-based approach allows for a direct assessment of the scaffolds' ability to produce •OH when exposed to an aqueous environment. Then the supernatant was collected, and the absorbance of MB at its characteristic absorption peak of 664 nm was measured using an ultraviolet-visible spectrophotometer.

### 2.9. Peroxidase-like activity of the scaffolds

Peroxidase-like activity was determined using the titanium sulfate colorimetric method: The initial step involved preparing a 5% $Ti(SO_4)_2$ solution. Three groups of scaffolds (PLLA, PLLA/NCDs, and PLLA/NCDs@MSN) were individually placed into a 6 mM $H_2O_2$ solution and incubated without agitation at room temperature for 15 min. This setup directly exposes the scaffolds to hydrogen peroxide in an aqueous medium, simulating the presence of bioavailable $H_2O_2$ within the body. Then, 0.1 mL of the reaction solution was aspirated and transferred into a 96-well plate, and 100 μL of titanium sulfate solution was then added to each group of wells. A multi-functional microplate reader (Fluoroskan FL, Thermo Fisher, USA) was used to measure the absorbance at 412 nm to evaluate the $H_2O_2$ consumption capacity of the scaffolds. Additionally, the absorbance changes of the PLLA/NCDs@MSN scaffold within 0–30 min of reaction were determined.

### 2.10. Cell culture

Human osteosarcoma cells (MG-63) and mouse bone marrow mesenchymal stem cells (BMMSCs) were provided by the Experimental Center of Central South University, China. Cells were resuspended in high-glucose Dulbecco's Modified Eagle Medium supplemented with 10% fetal bovine serum and 1% penicillin–streptomycin, after which they were seeded into culture dishes. MG-63 cells were cultured under normoxia (21% $O_2$, 5% $CO_2$, 37 °C) and hypoxia (2% $O_2$, 5% $CO_2$, 90% $N_2$, 37 °C) conditions, depending on the experimental design.

### 2.11. Intracellular antitumor performance

#### *2.11.1. Cellular reactive oxygen species assay*

Intracellular ROS levels were detected using the 2,7-dichlorodihydrofluorescein diacetate (DCFH-DA) probe (Beyotime Biotechnology Co., Ltd., China). MG-63 cells in the logarithmic growth phase were seeded into 24-well plates; when cell confluency reached 70–80% of the well area, they were co-cultured with sterilized scaffolds (two groups: light-irradiated and non-irradiated control). After co-culture, the cells were washed with phosphate-buffered saline (PBS). Then, 10 μM DCFH-DA probe solution was added, and the cells were incubated in normoxic and hypoxic environments for 30 min, respectively. After incubation, the cells were washed with phosphate-buffered saline (PBS), and finally, cellular fluorescence images were captured using a fluorescence microscope.

#### *2.11.2. Live/dead cell staining*

MG-63 cells were co-cultured with sterilized scaffolds (light-irradiated/non-irradiated control) in 96-well plates, then incubated in normoxic/hypoxic conditions for a specific time. Post-incubation, cells were gently rinsed with PBS to remove residual medium. Calcein acetoxymethyl ester (Calcein-AM)/propidium iodide (PI)

staining solution (Beyotime, Shanghai, China) was added, and plates were incubated at 37 °C in the dark for 20–30 min. Subsequently, the staining solution was aspirated, and unbound dyes were washed off with PBS. Cell images were captured via fluorescence microscope (BX51, Olympus, Japan), which showed viable cells as green fluorescence and dead cells as red fluorescence. Finally, ImageJ (https://imagej.net/ij/) was used to count the proportion of viable/total cells. The cell viability was calculated as:

$$\text{Viability}(\%)=\frac{\text{Viable}_{\text{cells}}}{\text{Total}_{\text{cells}}}\times 100 \quad (1)$$

### 2.12. Cell cytotoxicity evaluation

#### *2.12.1. Cellular morphology observation*

Cell morphological observation was performed via cell adhesion assay combined with SEM to evaluate the morphological characteristics of BMMSCs, after co-culture with three groups of scaffolds. BMMSCs were co-cultured with each group of scaffolds in a 37 °C, 5% $CO_2$ incubator for two days. Thereafter, the scaffolds were gently rinsed with PBS three times to remove non-adherent cells, followed by fixation with 4% paraformaldehyde at room temperature for 30 min. Subsequently, gradient ethanol solutions (30%, 50%, 75%, 80%, 90%, 95%, and 100% in sequence) were used for dehydration, with 5 min per concentration. Finally, the samples were observed under SEM to analyze the morphological characteristics of BMMSCs.

#### *2.12.2. Cell proliferation*

The CCK-8 assay was used to assess the viability of BMMSCs co-cultured with different scaffolds. BMMSCs ($1.5 \times 10^3$/well) were seeded in 96-well plates, cultured for 48 h (37 °C, 5% $CO_2$), followed by co-culturing with scaffolds for 1 or 3 days. After the culture period, the cells were washed with PBS, followed by adding 100 μL CCK-8 and incubating for 20–30 min. Optical density values at 450 nm were measured, and the cell viability was calculated using the following formula:

$$Viablity(\%)=\frac{OD_{experimental}-OD_{blank}}{OD_{control}-OD_{blank}}\times 100 \quad (2)$$

Triplicates and three independent repeats were performed. Furthermore, live/dead fluorescence staining was performed on BMMSCs co-cultured with scaffolds at 1 day or 3 days using Calcein-AM/PI. Stained cells were observed under the fluorescence microscope.

### 2.13. Statistical analysis

All experiments were conducted with three parallel samples, and the results were exhibited as mean ± standard deviation. All statistical analyses were carried out using Prism (Graphpad Prism 9.5, GraphPad, USA) and Origin (Origin 2024, OriginLab Corporation, USA). A $p$-value < 0.05 was considered statistically significant, and significance levels are indicated as $^{*}p < 0.05$, $^{**}p < 0.01$, $^{***}p < 0.001$, and $^{****}p < 0.0001$.

## 3. Results and discussion

### 3.1. Physicochemical characterization of synthesized nanoparticles

NCDs@MSN were synthesized using a hydrothermal method (Figure 1a).[18] TEM revealed that NCDs@MSN possessed mesoporous spherical morphologies with local aggregation (Figure 1b). EDS confirmed the uniform distribution of carbon (C), nitrogen (N), oxygen (O), and silicon (Si) within NCDs@MSN (Figure 1c), further verifying the successful synthesis of the NCDs@MSN. The high-resolution TEM image (Figure 1d) clearly demonstrated uniform dispersion of NCDs on the surface of MSN. Well-resolved lattice fringes with a spacing of 0.21 nm were observed in the fast Fourier transform pattern (Figure 1$d_1$), which were attributed to the (100) plane of the graphite structure.[19]

X-ray diffraction patterns were analyzed to characterize the crystalline phase and crystallinity. The broad peak around 25° of NCDs and NCDs@MSN, as presented in Figure 2a, was attributed to the graphite structure (002). Subsequently, $N_2$ adsorption–desorption measurements were performed to characterize the porous structure of NCDs@MSN. Its adsorption-desorption isotherm (Figure 2b) exhibited a typical Type IV profile, with a distinct H4-type hysteresis loop in the 0.4–1.0 $P/P_0$ range. This was a characteristic hallmark of mesoporous materials that aligned with the mesoporous morphology observed in prior TEM characterizations. Meanwhile, the corresponding pore size distribution (inset of Figure 2b) was narrow, with the main peak centered at 6.53 nm, confirming the material's relatively uniform mesoporous channel structure. Notably, mesoporous structures provided a large specific surface area and well-defined pores, and both attributes facilitated mass transfer and interfacial interactions during adsorption and catalysis processes.

Fourier transform infrared spectroscopy was employed to identify the functional groups on the surface of nanomaterials. In Figure 2c, both NCDs and NCDs@MSN displayed similar peaks at 3,433 $cm^{-1}$ and 3,426 $cm^{-1}$, corresponding to N–H stretching vibrations, and at 1,592 $cm^{-1}$ and 1,637 $cm^{-1}$, attributed to C=C stretching vibrations.[20,21] These results confirm the presence of a carbon core structure in both materials. Moreover, the

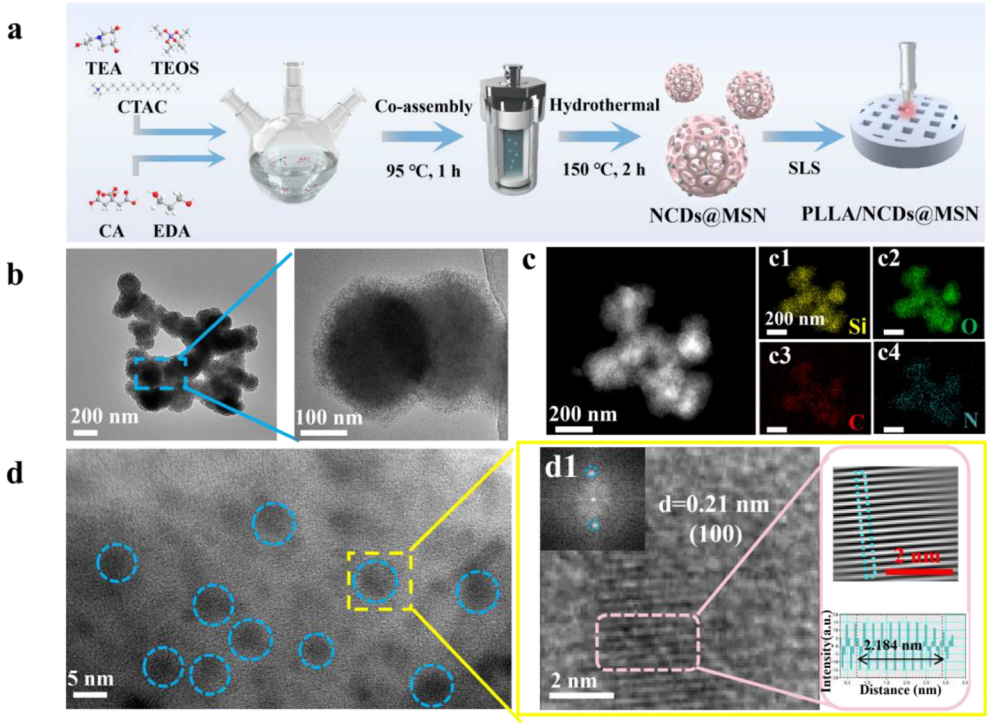


**Figure 1.** TEM of NCDs@MSN. (a) Schematic of the NCDs@MSN synthesis process. (b) TEM images of NCDs@MSN (left; scale bars: 200 nm; magnification: 20,000×) and its high-resolution TEM image (right; scale bars: 100 nm; magnification: 80,000×). (c) EDS mapping of NCDs@MSN (scale bars: 200 nm; magnification: 90,000×). (d) High-resolution TEM image (scale bars: 5 nm; magnification:800,000×) of NCDs@MSN showing uniformly dispersed NCDs on the MSN surface, together with ($d_1$) the Fourier transform pattern (corresponding to the area indicated by the yellow dashed box) (scale bars: 2 nm; magnification: 2,500,000. Blue circles indicate uniformly dispersed NCDs on the MSN surface.
Abbreviations: CA: Citric acid; CTAC: Cetyltrimethylammonium chloride; EDA: Ethylenediamine; EDS: Energy dispersive spectroscopy; SLS: Selective laser sintering; TEA: Triethanolamine; TEM: Transmission electron microscopy; TEOS: Tetraethyl orthosilicate.

peaks at 1,093 $cm^{-1}$ and 808 $cm^{-1}$, which corresponded to the stretching vibration of Si–O–Si bonds and Si–C,[22,23] demonstrated the presence of MSN in the composite and provided direct evidence for covalent Si–C bond formation. The zeta potential of NCDs was approximately 3 mV, while that of the NCDs@MSN composite measured around −5 mV (Figure 2d). The observed reversal in charge stemmed from the incorporation of MSN, which is linked to the partial dissociation of silanol groups (–Si–OH) on the surface of MSN in aqueous solution.[24] This process conferred a net negative charge to the composite.

X-ray photoelectron spectroscopy further verified the chemical compositions of pristine NCDs and the NCDs@MSN hybrid (Figure 2e). For NCDs@MSN, the signature binding energy peaks of C 1s, N 1s, and O 1s were consistent with those of pristine NCDs. Additionally, a distinct Si 2s peak was readily detected. This spectral evidence directly corroborated the successful immobilization of NCDs within the MSN matrix. Specifically, the high-resolution C 1s spectra of NCDs and NCDs@MSN (Figure 2f) each exhibited three deconvoluted peaks. For NCDs, the peaks were located at 284.8 eV (C–C/C=C), 286.3 eV (C–O), and 287.9 eV (C=O).[25] NCDs@MSN displayed peaks at 283.6 eV (Si–C), 284.2 eV (C–C/C=C), and 284.9 eV (C–O). The absence of the C=O peak and emergence of the Si–C peak in NCDs@MSN confirmed the formation of chemical bonding between NCDs and MSN.[26,27]

The N 1s band of NCDs and NCDs@MSN (Figure 2g) also showed three deconvoluted peaks but differed in nitrogen species. NCDs featured peaks at 399.6 eV (N–C), 400.7 eV (N–H), and 401.2 eV (N–O), while NCDs@MSN at 399.6 eV (pyridinic N), 401.5 eV (pyrrolic N), and 402.6 eV (graphitic N).[28,29] The transition confirmed the interaction between NCDs and MSN and implied nitrogen's electron-regulating role in the composite.

The O 1s XPS spectrum (Figure 2h) exhibited differences in deconvoluted peaks: NCDs displayed two peaks at 531.0 eV (C=O) and 532.2 eV (C–O),[30] whereas NCDs@MSN had three, retaining the C=O/C–O peaks with an additional peak at 533.3 eV (Si–O).[31] This new Si–O peak confirmed

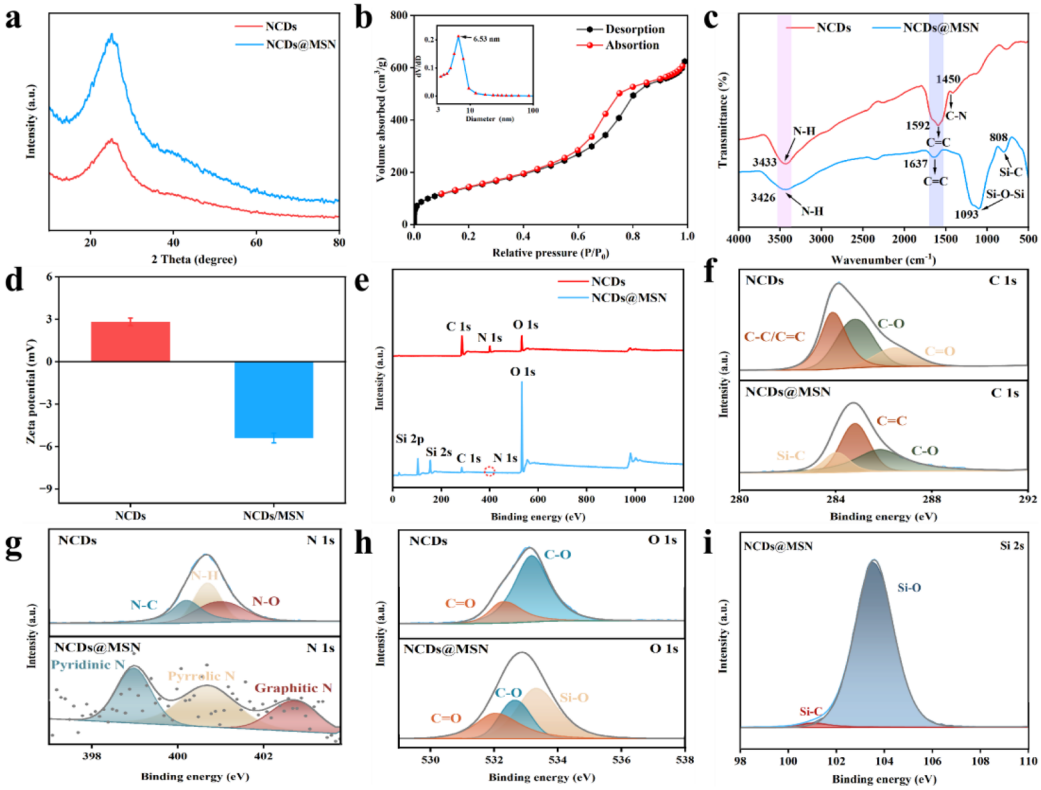


**Figure 2. Characterization of NCDs and NCDs@MSN**. (a) XRD patterns of NCDs and NCDs@MSN. (b) $N_2$ adsorption–desorption isotherm of NCDs@MSN. (c) Fourier transform infrared spectra of NCDs and NCDs@MSN. (d) Zeta potentials of NCDs and NCDs@MSN. (e) XPS survey spectra of NCDs and NCDs@MSN. High-resolution XPS spectra of (f) C 1s, (g) N 1s, and (h) O 1s for NCDs and NCDs@MSN, and (i) Si 2s for NCDs@MSN.
Abbreviations: XPS: X-ray photoelectron spectroscopy; XRD: X-ray diffraction.

successful MSN incorporation, while preservation of the C=O/C–O peaks verified the intact intrinsic structure of NCDs in the composite. The Si XPS spectra (Figure 2i) revealed two characteristic peaks at 101.1 eV (Si–C) and 103.2 eV (Si–O).[32] Notably, the Si–C peak matched the signal in the C 1s spectrum; furthermore, the Si–O peak validated retention of MSN's siloxane framework.

### 3.2. Photoresponsive catalytic property assessment

The fluorescence behavior of the NCDs@MSN was characterized by PL spectroscopy. The excitation wavelengths of NCDs and NCDs@MSN were 370 nm and 367 nm, respectively, and their emission wavelengths were 473 nm and 468 nm (Figure 3a). Additionally, the inset of Figure 3a displayed digital photographs of the two sample solutions under UV light, enabling a straightforward observation of the notable decrease in fluorescence intensity of NCDs@MSN. This reduction in fluorescence intensity was believed to stem from the partial aggregation of NCDs during their encapsulation into the MSN mesopores, leading to an aggregation-induced quenching effect that attenuated the fluorescence emission. These changes in fluorescence characteristics provided additional evidence supporting the effective integration of NCDs with MSNs. The NCDs@MSN also exhibited excitation-independent behavior (Figure 3b).

To verify the photoresponse capability of NCDs and NCDs@MSN, the UV/Vis absorption spectra of the samples are shown in Figure 3c. Both samples exhibited a broad absorption peak in the 400–800 nm visible light region, indicating that both materials had visible light response capabilities, which provided an important basis for their application in visible light-driven photocatalytic reactions. The band gap value of the samples could be estimated by Tauc plots derived from the Kubellka–Munk function. The specific formula is as follows: [33]

$$(\alpha hv)^{1/n}=A(hv-Eg) \quad (3)$$

where $\alpha$ represents the absorbance, $h$ denotes Planck's constant, $v$ is the frequency of light, $Eg$ stands for the semiconductor band gap width, $A$ is a constant related to the transition probability, and $n$ takes the value of 1/2 for

direct band gaps and 2 for indirect band gaps.[34,35] Calculated by the tangent intercept method, the band gap of NCDs was 3.03 eV, while that of NCDs@MSN was significantly reduced to 1.38 eV (Figure 3d). The narrow band gap of NCDs@MSN enabled electron transition under visible light energy, which not only promoted the generation of photogenerated carriers but also further enhanced the photocatalytic activity of the material.

The Mott–Schottky spectra were tested to evaluate the semiconductor type of NCDs and NCDs@MSN. As shown in Figure 3e, NCDs and NCDs@MSN presented typical characteristics of an n-type semiconductor due to the positive spectral slope,[36] and the conduction band edge potentials ($E_{CBM}$, vs. NHE) were determined to be −0.713 eV for NCDs and −0.883 eV for NCDs@MSN ($E_{CBM}$= $E_{fb}$ −0.2 eV; $E_{fb(NHE)}$ = $E_{fb(Ag/AgCl)}$ + 0.197, $E_{fb\ (NHE)}$ values were −0.513 eV for NCDs and −0.683 eV for NCDs@MSN).[37] The maximum valence band potentials ($E_{VBM(NHE)}$) were determined to be 2.317 eV for NCDs and 0.497 eV for NCDs@MSN (Eg = $E_{VBM}$ − $E_{CBM}$, $Eg_{NCDs}$ = 3.03 eV, $Eg_{(NCDs@MSN)}$ = 1.38 eV).[38]

Based on literature reports, a band model was constructed (Figure 3f). The reduction potential for $O_2$ + $e^-$ → $\bullet O_2^-$ is −0.33 eV (vs. NHE).[39] $E_{CB(NHE)}$ values of both NCDs and NCDs@MSN were more negative than −0.33 eV, indicating that photogenerated electrons in the conduction band could thermodynamically transfer spontaneously to $O_2$ and thereby reduce it to superoxide radicals ($\bullet O_2^-$). It is known that the oxidation potential of $H_2O$ to •OH is +2.01 eV (vs. NHE).[40] A comparison of the valence band potentials indicated that the $E_{VBM\ (NHE)}$ of NCDs@MSN was 0.497 eV, which was much lower than 2.01 eV, suggesting that the photogenerated holes in its valence band could not thermodynamically drive the reaction $H_2O$ → •OH. In contrast, the $E_{VBM\ (NHE)}$ of NCDs was 2.317 eV, which was close to 2.01 eV, indicating its potential to oxidize water to

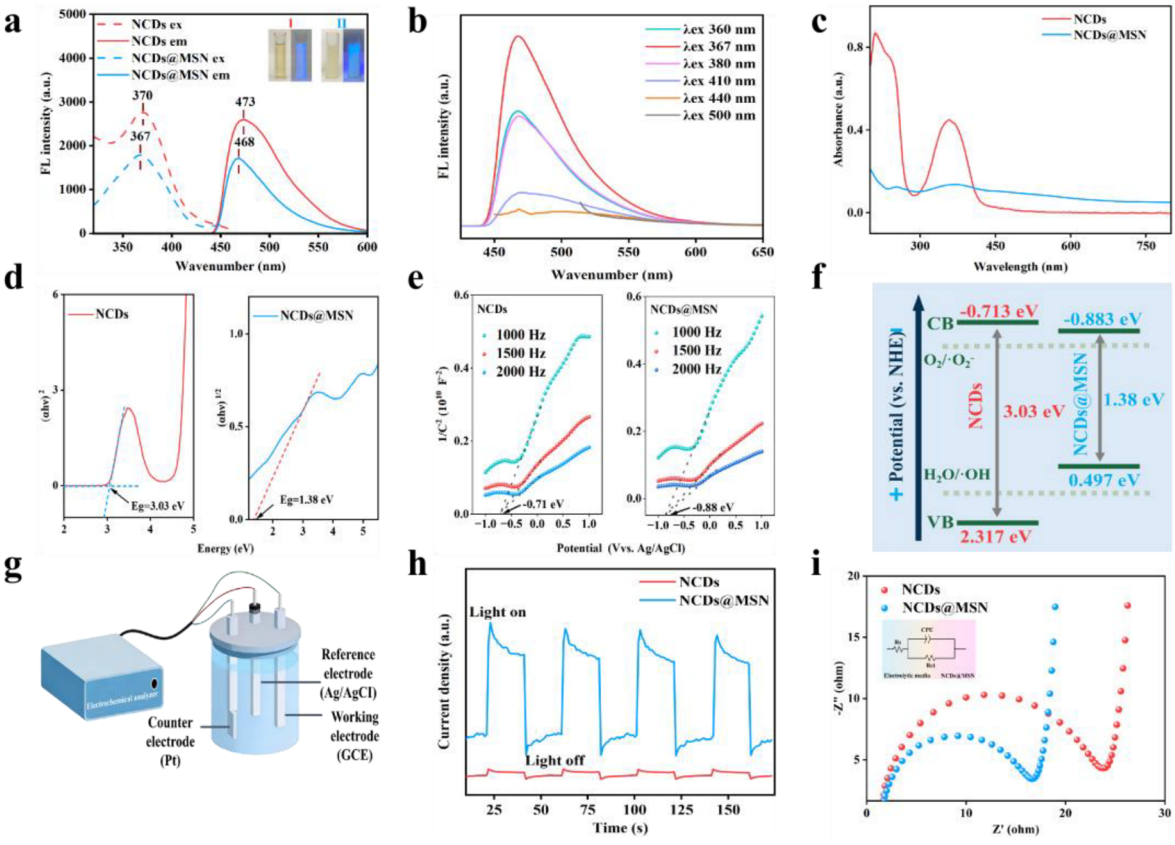


**Figure 3.** Photoelectrochemical characterization of NCDs and NCDs@MSN. (a) Excitation, emission spectra, and optical photographs (inset). (b) Emission spectra corresponding to excitation wavelengths in the range of 400–650 nm. (c) UV–Vis absorption spectra and (d) Tauc plots. (e) Mott–Schottky plot. (f) Electronic energy band model. (g) The electrochemical working model. (h) Transient photocurrent density versus irradiation time curve and (i) Electrochemical impedance spectroscopy spectra.
Abbreviation: FL: Fluorescence.

•OH.

To further assess the charge-transfer properties of NCDs@MSN, we conducted transient photocurrent generation and electrochemical impedance spectroscopy. The electrochemical working model was illustrated in Figure 3g. Figure 3h demonstrated the prompt and reproducible transient photocurrent responses across all samples. The photocurrent density generated by NCDs@MSN remained significantly higher than that of NCDs, thereby confirming the efficient separation of electron-hole pairs in NCDs@MSN. In the Nyquist plot presented in Figure 3i, the radius of the semicircle in the high-frequency region was directly associated with interfacial charge transfer resistance, where a smaller radius indicated a lower charge transfer resistance.[41] The results revealed that the semicircle radius of NCDs@MSN was notably smaller than that of NCDs, demonstrating a more efficient charge transfer process at the interface. This characteristic was conducive to enhancing the charge transfer efficiency in photocatalytic reactions, thereby improving the overall photocatalytic performance.

Ultimately, after the separation of photoexcited electron-hole pairs, NCDs@MSN demonstrated the ability to reduce $O_2$ to $\bullet O_2^-$ with high charge transfer efficiency. This observation provided crucial theoretical support for its application as a Type I photosensitizer.[42]

### 3.3. Characterization of the scaffolds

Building on the exceptional Type I photosensitizer characteristics of NCDs@MSN, this study successfully integrated the NCDs@MSN powder into the porous PLLA scaffolds using SLS. The intrinsic porous architecture of the PLLA scaffold, featuring interconnected pores averaging 600 μm (demonstrated by SEM imaging in Figure S1b–d), is crucial for the subsequent functional performance.

To confirm the successful integration and distribution of NCDs@MSN within the PLLA matrix, EDS elemental mapping was performed (Figure S1). The resulting elemental maps for Si, O, C, and N unequivocally demonstrate a homogeneous distribution of these elements originating from NCDs@MSN throughout the PLLA scaffold. Crucially, the intensity profiles exhibit minimal variation across different regions, providing strong evidence for the absence of significant aggregation or regional enrichment of the NCDs@MSN composite. This uniform dispersion, achieved through our optimized SLS fabrication process, ensures the stable incorporation of NCDs@MSN and guarantees adequate functional exposure and accessibility of the photosensitizer throughout the scaffold structure.

This homogeneous distribution is critical for efficient PDT. Upon light irradiation, the uniformly dispersed NCDs@MSN can generate ROS from multiple locations within the scaffold. The interconnected porous network then actively facilitates the diffusion of these generated ROS to the tumor microenvironment,[43] which is essential for localized and effective photodynamic antitumor activity. Therefore, the well-dispersed NCDs@MSN within the porous scaffold collectively contribute to robust photodynamic therapeutic outcomes.

Sufficient mechanical strength is paramount for bone scaffolds, ensuring they resist collapse and fracture post-implantation and thereby provide a stable three-dimensional microenvironment conducive to cell adhesion, proliferation, and subsequent bone tissue regeneration.[44] In this study, we systematically investigated the mechanical properties of each scaffold group. The compressive strengths of PLLA, PLLA/NCDs, and PLLA/NCDs@MSN scaffolds were determined to be 17.72 ± 1.21 MPa, 20.94 ± 3.40 MPa, and 27.73 ± 4.40 MPa, respectively. Similarly, the tensile strengths were measured to be 11.99 ± 0.24 MPa, 15.16 ± 0.07 MPa, and 19.69 ± 1.65 MPa, respectively (as illustrated in Figure S2).

Following modification with nanoparticles, a significant enhancement in the mechanical properties of the composite scaffolds was observed. Their compressive strengths favorably exceeded the reported range of cancellous bone (2–12 MPa),[45] providing sufficient mechanical support and preventing premature scaffold failure. Meanwhile, the compressive elastic modulus of the composite scaffolds fell within the physiological range of cancellous bone (11–24 MPa).[46] This crucial matching of elastic moduli is vital for mitigating the stress-shielding effect, thereby facilitating normal physiological bone tissue activities. Collectively, these findings underscore that the PLLA/NCDs@MSN scaffold exhibits excellent mechanical properties that meet the application requirements for bone implant scaffolds.

### 3.4. Reactive oxygen species generation and peroxidase-like activity analysis

The uniformly distributed nanoparticles in the scaffold, combined with the interconnected porous structure, facilitated the effective generation and diffusion of ROS. It was anticipated that the sustained and controlled release behavior of the PLLA/NCDs@MSN scaffold would not only achieve efficient PDT-mediated antitumor effects but also maintain stable enzymatic activity, which would provide a novel strategy for the long-term and precise management of bone tumors.

#### *3.4.1. Reactive oxygen species detection*

To explore and compare the photodynamic performance

of PLLA, PLLA/NCDs, PLLA/NCDs/MSN, and PLLA/NCDs@MSN scaffolds, NBT and MB were employed as probes for $\bullet O_2^-$ and •OH, respectively. Among them, the pale yellow NBT reacted with $\bullet O_2^-$ to form blue formazan, whose characteristic absorption peak was around 560 nm. As a strong oxidant, •OH underwent oxidative reaction with MB, causing the intensity of MB's characteristic absorption peak (typically around 664 nm) to decrease with increasing •OH concentration.

The highest absorption peak at 560 nm was observed in the PLLA/NCDs@MSN group, demonstrating its potent $\bullet O_2^-$ generation capability compared to other scaffolds (Figure 4a), and the relative intensity of this peak increased significantly over time (Figure 4b), demonstrating that the scaffold-triggered ROS production was positively correlated with light irradiation. Subsequently, the PLLA/NCDs@MSN group exhibited the lowest absorption peak among the four groups (Figure 4c), indicating its strongest •OH-generating capacity. In Figure 4d, the peak intensity of the scaffold exhibited a significant decline over time, indicating that the •OH generation process of the scaffold was characterized by time dependence. Moreover, electron spin resonance confirmed that the PLLA/NCDs@MSN scaffold could generate $\bullet O_2^-$ (characteristic 1:1:1:1 peaks; Figure 4e) and •OH (characteristic 1:2:2:1 peaks; Figure 4f) under light irradiation, with the radical signal intensity

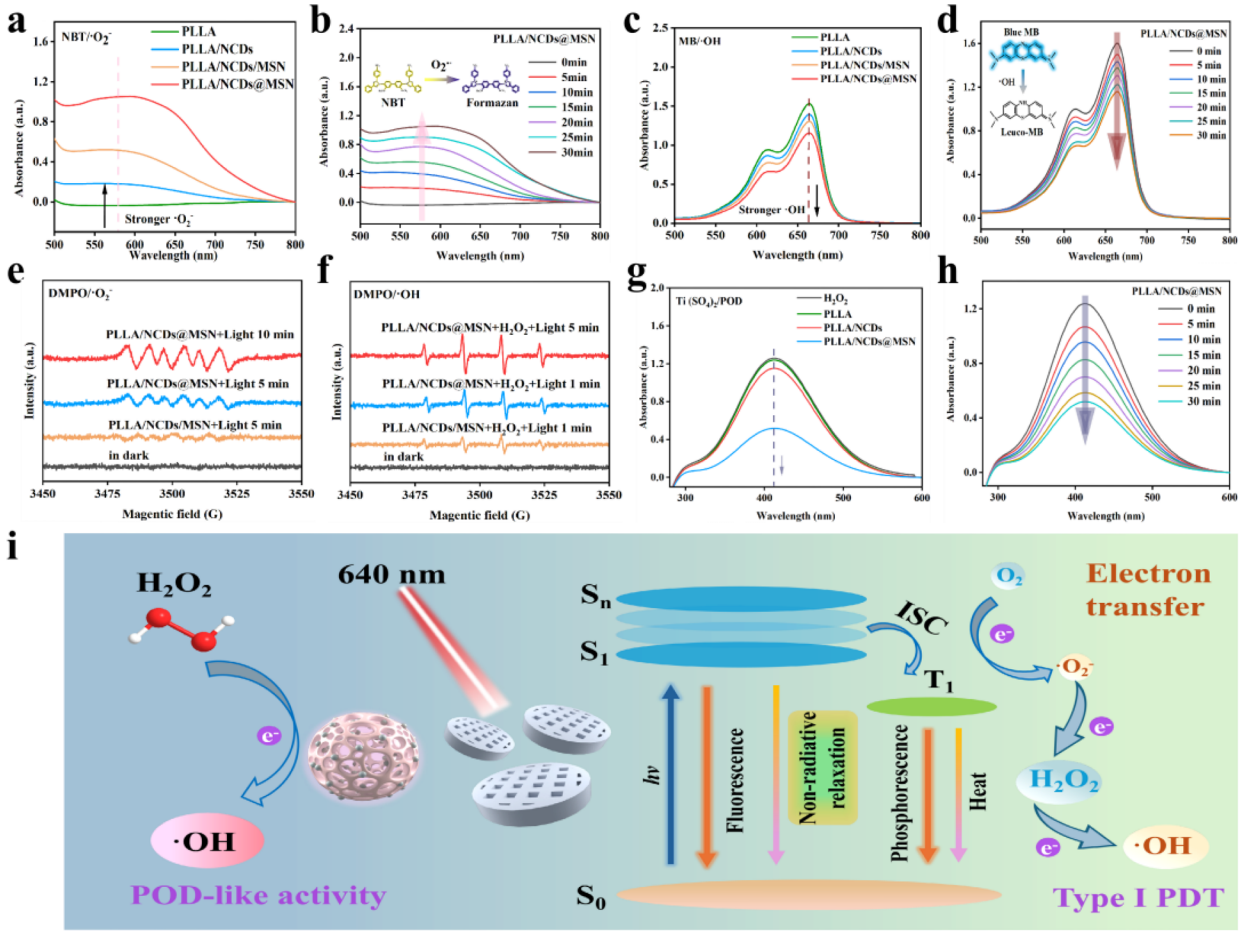


**Figure 4.** Evaluation of ROS generation of scaffolds. (a) Detection of $\bullet O_2^-$ of scaffolds and (b) detection of $\bullet O_2^-$ of the PLLA/NCDs@MSN scaffold at different times (inset: schematic diagram of NBT reaction mechanism). (c) Detection of •OH of scaffolds and (d) detection of •OH of the PLLA/NCDs@MSN scaffold at different times (inset: schematic diagram of MB reaction mechanism). Electron spin resonance spectra of (e) $\bullet O_2^-$ and (f) •OH. (g) Residual $H_2O_2$ detection during POD-like catalysis. (h) Time-dependent residual $H_2O_2$ detection for the PLLA/NCDs@MSN scaffold. (i) Schematic illustration of reactive oxygen species generation mechanisms.

Abbreviations: DMPO: 5,5-dimethyl-1-pyrroline N-oxide; ISC: Intersystem crossing; MB: Methylene blue; NBT: Nitroblue tetrazolium; PDT: Photodynamic therapy; PLLA: poly-L-lactic acid; POD: Peroxidase.

increased over time, indicating its ability to sustainably produce ROS. These results indicated that PLLA/NCDs/MSN generated more ROS than PLLA/NCDs, confirming that the mesoporous confinement and dispersion effects of MSN enhanced ROS production. Meanwhile, PLLA/NCDs@MSN exhibited significantly higher ROS yields than PLLA/NCDs/MSN. Accordingly, although physical confinement by MSN improved the photodynamic performance of NCDs, the Si–C covalent bonds between NCDs and MSN were the dominant factor. These bonds provided efficient charge transfer channels and suppressed the recombination of photogenerated electron-hole pairs, which further validated the superiority of PLLA/NCDs@MSN for efficient and sustained ROS generation via the type I mechanism.

#### *3.4.2. Peroxidase-like activity*

Endogenous $H_2O_2$ levels in tumor cells are significantly higher than those in normal cells; this abnormal elevation promotes the proliferation and migration of tumor cells.[47] POD-like nanozymes are nanomaterials that mimic the catalytic activity of natural PODs. Notably, their key distinguishing feature is their capacity to catalyze the decomposition of $H_2O_2$ in the acidic tumor microenvironment, generating highly oxidative species such as •OH radicals.[48]

Herein, a scaffold with remarkable POD-like catalytic activity was developed, and its catalytic performance was validated. Specifically, titanium sulfate [$Ti(SO_4)_2$] was used as a colorimetric reagent to evaluate the peroxidase-like (POD-like) activity. $Ti(SO_4)_2$ can react with $H_2O_2$ to form a yellow-orange precipitate. The scaffold consumed $H_2O_2$ to generate •OH, thereby reducing the amount of $H_2O_2$ available for the above reaction. This change was reflected by a significant decrease in the intensity of the characteristic absorption peak at 412 nm in the UV-Vis spectrum.[49] The scaffold consumed $H_2O_2$ to generate •OH, directly reducing precipitate formation from the $Ti(SO_4)_2$–$H_2O_2$ reaction, which was reflected in a notable reduction in the 412 nm characteristic absorption peak intensity in the UV-visible spectrum. The PLLA/NCDs@MSN scaffold showed the lowest peak intensity (Figure 4g), confirming its stronger $H_2O_2$ consumption capacity and superior POD-like activity.

Subsequently, dynamic experiments (Figure 4h) demonstrated that the scaffold's absorbance decreased continuously with extended irradiation time, confirming that the PLLA/NCDs@MSN scaffold exhibits long term POD-like activity. Structurally, MSN's stable framework and uniform pores inhibited NCDs aggregation and modulated the photoresponse of the material, which may have further enhanced its POD-like activity.

The ROS generation mechanism of the PLLA/NCDs@MSN scaffold is illustrated in Figure 4i. Because PLLA/NCDs@MSN had a narrow band gap (1.38 eV), visible-light irradiation at 640 nm excites valence-band electrons and promotes their transfer to the conduction band. Excited electrons reduced $O_2$ to $\bullet O_2^-$, which subsequently partially participate in a two-electron reduction that contribute to •OH formation.

### 3.5. *In vitro* antitumor performance

In this study, DCFH-DA was selected as the green fluorescent probe to evaluate the scaffold's ROS-generating performance in tumor cells.[50] Fluorescence microscopy observations showed that MG-63 cells treated with light alone exhibited no fluorescent signal, whereas all MG-63 cells treated with the scaffold (under light irradiation) displayed green fluorescent signals. In normoxic conditions, intracellular fluorescence intensity was higher in the PLLA/NCDs@MSN group than the PLLA/NCDs group under light irradiation (Figure 5a). Quantitative analysis of fluorescence intensity via ImageJ software revealed that the fluorescence intensity of hypoxic MG-63 cells treated with the PLLA/NCDs@MSN scaffold was comparable to that of normoxic cells (Figure 5b), providing direct evidence for the scaffold's ROS-generating effect in hypoxic tumors.

Subsequently, the *in vitro* antitumor efficacy of the prepared scaffolds was evaluated via live/dead cell staining analysis. Tumor cells co-cultured with different scaffolds were stained and analyzed via a Calcein-AM/PI dual-fluorescence probe system.[51] Under light irradiation, MG-63 cells (normoxic/hypoxic) treated with PLLA/NCDs@MSN exhibited significantly increased red fluorescence and decreased green fluorescence compared with the PLLA/NCDs group (Figure 5c). This directly confirmed that PLLA/NCDs@MSN more effectively induced tumor cell death and exerted strong cytotoxicity under both oxygen conditions. In contrast, under non-irradiated conditions, sparse red fluorescence (with dominant green fluorescence) was observed in cells treated with either scaffold, which indicated only partial tumor cell death and limited cytotoxic efficiency of both scaffolds in the absence of light.

In addition, the cell viability results obtained were consistent with the overall trend observed in this live/dead cell staining assay (Figure 5d). This further confirmed that the PLLA/NCDs@MSN scaffold exhibited excellent cytotoxicity toward tumor cells, including those in hypoxic environments under light irradiation, providing a solid cellular experimental basis for its subsequent antitumor applications.

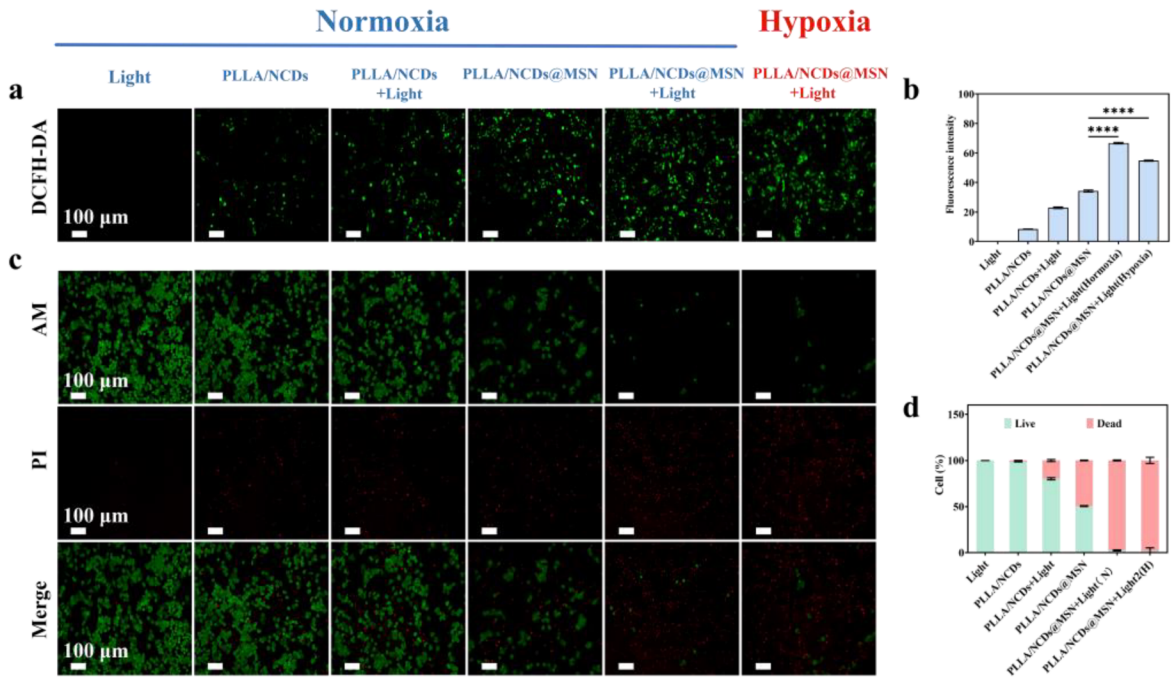


**Figure 5.** In vitro anti-tumor activity and intracellular ROS analysis of the scaffold. (a) Reactive oxygen species (ROS) fluorescence staining and (b) ROS fluorescence intensity. (c) Live/dead fluorescent images. (d) Cell viability. Scale bars: 100 μm; magnification: 20×.

Upon 640 nm light excitation, the PLLA/NCDs@MSN scaffold interacted with intracellular substrates and molecular oxygen in tumor cells via a type I PDT pathway, generating ROS such as $\bullet O_2^-$ and •OH (Figure 6). These ROS not only directly induced oxidative damage to tumor cells but also compromised mitochondrial function, thereby triggering the release of endogenous $H_2O_2$, which served as a crucial substrate for the scaffold-mediated POD reaction, leading to the production of additional •OH. Such synergy with PDT achieved enhanced overall antitumor efficacy. Notably, this process was independent of exogenous oxygen supply, thus effectively overcoming the constraints imposed by the tumor hypoxic microenvironment on traditional PDT.

### 3.6. Biocompatibility evaluation

Bone marrow mesenchymal stem cells were co-cultured with the PLLA, PLLA/NCDs, and PLLA/NCDs@MSN scaffolds for 24 h, then their cell morphology was observed via SEM. All scaffolds exhibited robust adhesion (Figure 7a). Most cells spread extensively on the scaffold surfaces, displaying typical polygonal or spindle-shaped morphologies that were consistent with the normal phenotype of undifferentiated stem cells. The cell membranes remained intact, with distinct pseudopodia extending to anchor firmly to the scaffolds, which provided evidence of stable cell–scaffold interactions.[52] Moreover, no significant number of floating cells or apoptotic features were observed. Collectively, these findings confirmed that the PLLA, PLLA/NCDs, and PLLA/NCDs@MSN scaffolds all possessed favorable biocompatibility to support stem cell adhesion.

The biocompatibility of the scaffolds was further assessed. Live/dead cell staining demonstrated that after 72 h of culture, all three scaffold groups had a high percentage of viable green-stained cells, and no distinct red fluorescence was observed (Figure 7b). The CCK-8 assay quantified the proliferative activity of BMMSCs,[53] after 3 days, all groups exhibited increased absorbance, with the PLLA/NCDs@MSN group marginally lower than the other two groups (Figure 7c). Collectively, the three scaffolds supported BMMSC survival and proliferation, possessing favorable biocompatibility.

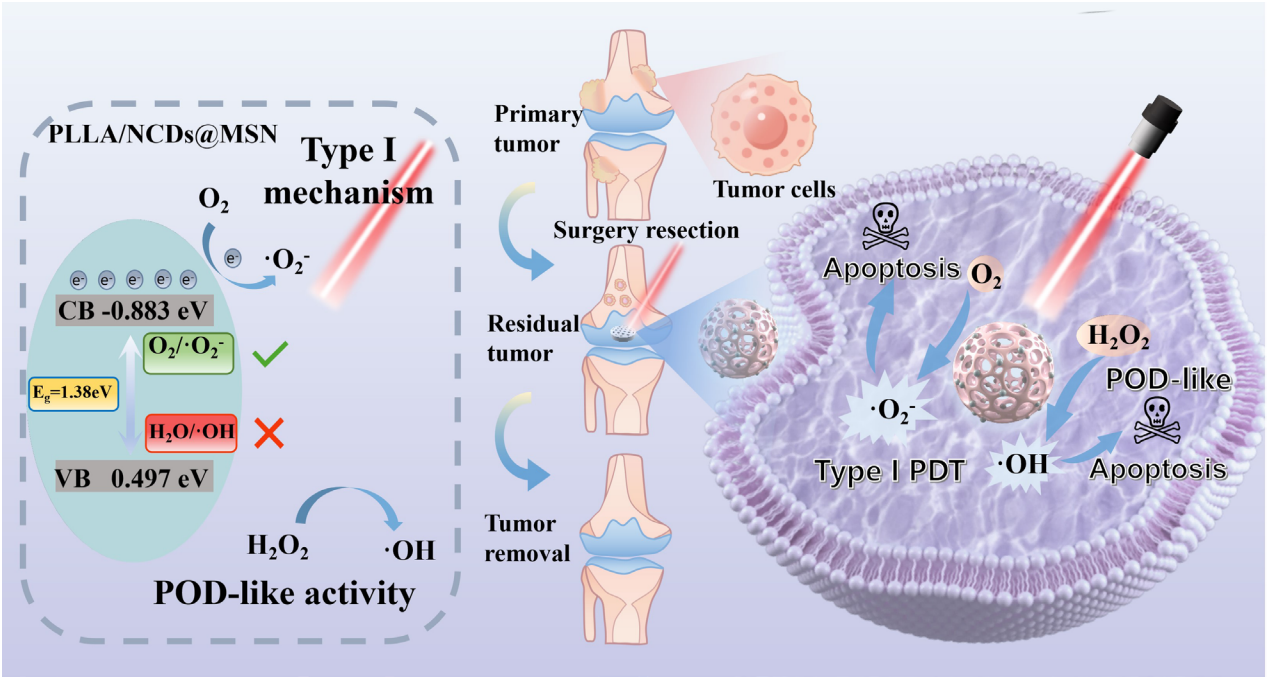


**Figure 6.** Schematic illustration of the synergistic antitumor mechanism of type I photodynamic therapy and the enzymatic reaction induced by the NCDs@MSN/PLLA composite scaffold.
Abbreviations: CB: Conduction band; PDT: Photodynamic therapy; POD: Peroxidase.

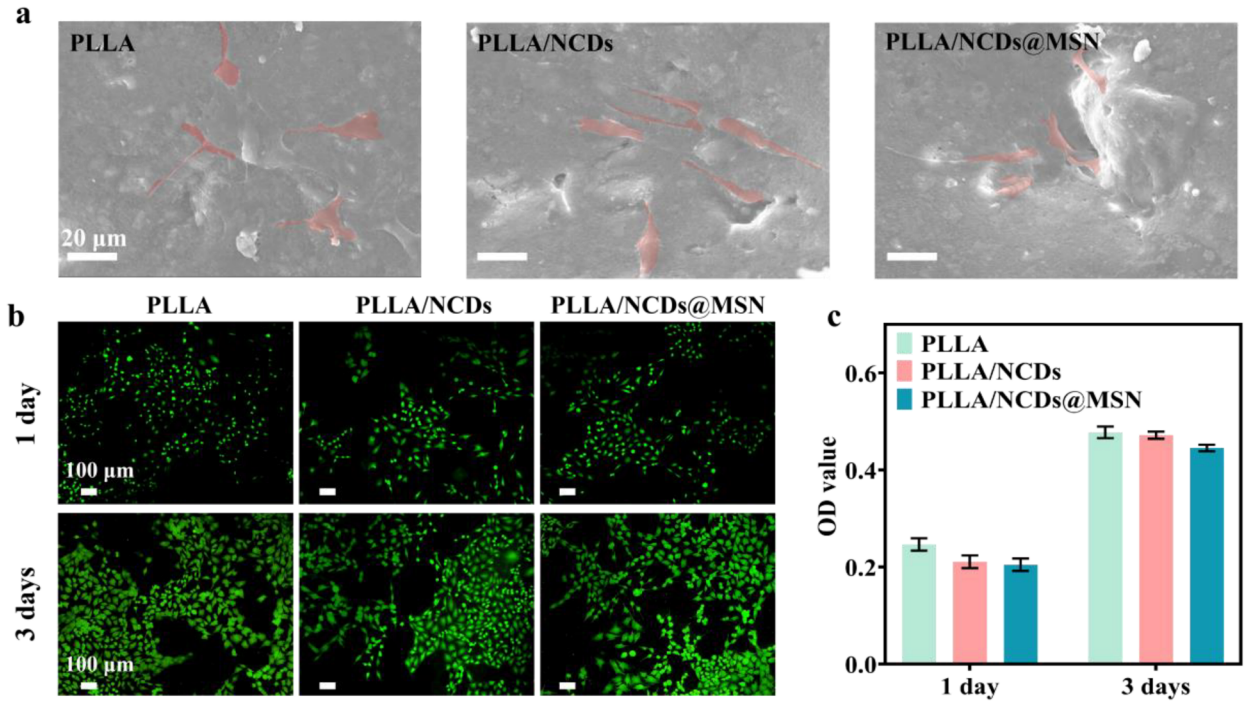


**Figure 7.** Biocompatibility Assessment of the Scaffolds. (a) Morphological characteristics of bone marrow mesenchymal stem cells (BMMSCs) cultured on different scaffolds. (b) Fluorescence live/dead staining analysis of BMMSCs cultured on varied scaffolds and (c) CCK-8 assay.

## 4. Conclusion

In this study, a type I photosensitizer (NCDs@MSN) was synthesized and incorporated into PLLA bone scaffolds to endow PDT antitumor functionality. NCDs@MSN, with its narrow band gap and covalent Si–C bonding, facilitated interfacial electron transfer and generated abundant $\bullet O_2^-$ and •OH under hypoxic conditions. Moreover, NCDs@MSN exhibited POD activity, catalyzing endogenous $H_2O_2$ to produce additional •OH, synergistically amplifying the antitumor effect of the PLLA/NCDs@MSN scaffold. Electrochemical impedance spectroscopy showed reduced interfacial resistance, and transient photocurrent measurements showed enhanced charge separation. The electron spin resonance curves have demonstrated the excellent ROS generation ability of NCDs@MSN. The antitumor efficacy of the PLLA/NCDs@MSN scaffold was confirmed by a tumor cell apoptosis rate of over 95% in the model assay, which is attributed to its efficient ROS-generating capability. Additionally, the biocompatibility of the PLLA/NCDs@MSN scaffold and its ability to support cell proliferation were assessed by cell-adhesion analysis, fluorescence staining, and CCK-8 assays.

## Acknowledgments

None

## Funding

This work was financially supported by the National Key Research and Development Program of China (grant no.: 2023YFB4605800); the Natural Science Foundation of China (grant nos.: U24A20120, 52475362, 52365046, 52465041); JiangXi Provincial Natural Science Foundation of China (grant nos.: 20224ACB204013, 20252BAC240111); Jiangxi Provincial Key Laboratory of Additive Manufacturing of Implantable Medical Device (grant no.: 2024SSY11161); and Jiangxi Provincial Department of Education Science and Technology Project (grant no.: GJJ2200813). All funders have no influence on the study design, execution, data interpretation, or the content of the published article.

## Conflict of interest

The authors declare that they have no known competing financial interests or personal relationships that could have appeared to influence the work reported in this paper.

## Author contributions

*Conceptualization:* Cijun Shuai
*Formal analysis:* Zhiheng Yu
*Investigation:* Weifan Dai, Jiaxiang Wu
*Methodology:* Shuping Peng
*Writing–original draft:* Bingxin Sun
*Writing–review & editing:* Guoyong Wang

## Ethics approval and consent to participate

The mouse bone marrow mesenchymal stem cells (BMSCs) were used solely for in vitro biocompatibility assessments. No in vivo animal experiments or manipulations involving live animals were conducted. In line with common ethical guidelines for laboratory animal research, such in vitro cell culture studies do not require additional animal ethics committee approval.

## Consent for publication

Not applicable.

## Availability of data

All data used in this study are available from the corresponding author upon reasonable request.

## Reference

1. Abad-Montero D, Gandioso A, Izquierdo-García E, *et al*. Ruthenium(II) polypyridyl complexes containing COUBPY ligands as potent photosensitizers for the efficient phototherapy of hypoxic tumors. *J Am Chem Soc*. 2025;147(9):7360-7376.

   doi: 10.1021/jacs.4c15036

2. Nosaka Y, Nosaka AY. Generation and Detection of Reactive Oxygen Species in Photocatalysis. *Chem Rev*. 2017;117(17):11302-11336.

   doi: 10.1021/acs.chemrev.7b00161

3. Shuai C, Li D, Xie H, Yao X, Peng S, Gao C. Programmable lamellar eutectic Zn-2Al-Mg biodegradable implants manufactured by laser powder bed fusion for synergistic strength-ductility and osteogenesis. *Adv Healthc Mater*. 2025;14(32):2501917.

   doi: 10.1002/adhm.202501917

4. Lin Y, Wu S, Li X, *et al*. Microstructure and performance of Z-scheme photocatalyst of silver phosphate modified by MWCNTs and Cr-doped SrTiO3 for malachite green degradation. *Appl Catal B*. 2018;227:557-570.

   doi: 10.1016/j.apcatb.2018.01.054

5. Li D, Xie H, Gao C, Jiang H, Wang L, Shuai C. Harmonic heterostructured pure Ti fabricated by laser powder bed fusion for excellent wear resistance via strength-plasticity synergy. *Opto-Electron Adv*. 2025;8(9):250043.

   doi: 10.29026/oea.2025.250043

6. Li Z, Zhang T, Fan F, Gao F, Ji H, Yang L. Piezoelectric materials as sonodynamic sensitizers to safely ablate tumors: a case study using black phosphorus. *J Phys Chem Lett*. 2020;11(4):1228-1238.

doi: 10.1021/acs.jpclett.9b03769

7. Lu S, Yang B. Carbon dots are shining in the world. *SmartMat*. 2022;3(2):207.

   doi: 10.1002/smm2.1132

8. Gao X, Tan J, Ye T, *et al*. Ti3C2Tx-enhanced photo-thermoelectric performance of Bi2Te3 in scaffold for improved osteogenic potential. *J Colloid Interface Sci*. 2026;702:138794.

   doi: 10.1016/j.jcis.2025.138794

9. Shuai C, Pan G, Wang Z, *et al*. Bifunctional MoS2@Cu2O heterojunction within scaffold for dual-mode synergistic antibacterial effects. *Appl Surf Sci*. 2025;686:162154.

   doi: 10.1016/j.apsusc.2024.162154

10. Zhang Z, Song S, Ding Y, *et al*. Ultrasonic enhanced liquid-liquid interfacial reaction for improving the synthesis of Iron-doped carbon dots (Fe-CDs) for achieving superior photocatalytic performance. *J Colloid Interface Sci*. 2024;669:816-824.

    doi: 10.1016/j.jcis.2024.05.070

11. Kurdyukov DA, Eurov DA, Stovpiaga EY, *et al*. Novel solid state of silica with ultra-high specific surface area. *Mater Today*. 2025;88:146-154.

    doi: 10.1016/j.mattod.2025.06.006

12. Tang X, Wu Y, Shen Y, *et al*. Heterogeneous-structure-based AuNBs@TiO2 nano-photosensitizers for computed tomography imaging guided NIR-II photodynamic therapy and cancer metastatic prevention. *Adv Healthc Mater*. 2024;13(18):2304209.

    doi: 10.1002/adhm.202304209

13. Lee H, Han G, Na Y, *et al*. 3D-printed tissue-specific nanospike-based adhesive materials for time-regulated synergistic tumor therapy and tissue regeneration in vivo. *Adv Funct Mater*. 2024;34(48):2406237.

    doi: 10.1002/adfm.202406237

14. Tian B, Liu S, Yu C, *et al*. A metal-free mesoporous carbon dots/silica hybrid type I photosensitizer with enzyme-activity for synergistic treatment of hypoxic tumor. *Adv Funct Mater*. 2023;33(25):2300818.

    doi: 10.1002/adfm.202300818

15. Wang L, Zhang H, Zhou X, Liu Y, Lei B. Preparation, characterization and oxygen sensing properties of luminescent carbon dots assembled mesoporous silica microspheres. *J Colloid Interface Sci*. 2016;478:256-262.

    doi: 10.1016/j.jcis.2016.06.026

16. Shuai X, Yang Y, Qi F, Yang M, Shuai C. Phase-field modeling of laser sintering degradable biopolymer. *Compos Commun*. 2025;53:102244.

    doi: 10.1016/j.coco.2024.102244

17. Sun B, Peng S, Zhang Z, *et al*. A bifunctional scaffold achieves a two-stage strategy for repairing tumorous bone defects. *Colloids Surf A Physicochem Eng Asp*. 2025;726:137996.

    doi: 10.1016/j.colsurfa.2025.137996

18. Aebisher D, Czech S, Dynarowicz K, *et al*. Photodynamic therapy: past, current, and future. *Int J Mol Sci*. 2024;25(20):11325.

    doi: 10.3390/ijms252011325

19. Aebisher D, Szpara J, Bartusik-Aebisher D. Advances in medicine: photodynamic therapy. *Int J Mol Sci*. 2024;25(15):8258.

    doi: 10.3390/ijms25158258

20. Blasi M, Pagliara M, Lanza A, *et al*. Photodynamic Therapy in Ocular Oncology. *Biomedicines*. 2018;6(1):17.

    doi: 10.3390/biomedicines6010017

21. Chou W, Sun T, Peng N, *et al*. Photodynamic therapy-induced anti-tumor immunity: influence factors and synergistic enhancement strategies. *Pharmaceutics*. 2023;15(11):2617.

    doi: 10.3390/pharmaceutics15112617

22. Cramer GM, Cengel KA, Busch TM. Forging forward in photodynamic therapy. *Cancer Res*. 2022;82(4):534-536.

    doi: 10.1158/0008-5472.Can-21-4122

23. Qu J, Zhou W, Zhang W, *et al*. Tunable time-dependent phosphorescent colors and evolution direction of solvent-free grown carbon dots within hollow mesoporous silica for dynamic information encryption. *Chem Eng J*. 2025;524:169198.

    doi: 10.1016/j.cej.2025.169198

24. Cui X, Li X, Peng C, *et al*. Beyond external light: on-spot light generation or light delivery for highly penetrated photodynamic therapy. *ACS Nano*. 2023;17(21):20776-20803.

    doi: 10.1021/acsnano.3c05619

25. Ren Y, Fan Z. Synthesis of fluorescent probe based on molecularly imprinted polymers on nitrogen-doped carbon dots for determination of tobramycin in milk. *Food Chem*. 2023;416:135792.

    doi: 10.1016/j.foodchem.2023.135792

26. Hang L, Zhang T, Wen H, *et al*. Controllable photodynamic performance via an acidic microenvironment based on two-dimensional metal-organic frameworks for photodynamic therapy. *Nano Res*. 2021;14(3):660-666.

    doi: 10.1007/s12274-020-3093-1

27. Ye J, Miao B, Xiong Y, *et al*. 3D printed porous magnesium metal scaffolds with bioactive coating for bone defect repair: enhancing angiogenesis and osteogenesis. *J Nanobiotechnology*. 2025;23(1):355.

doi: 10.1186/s12951-025-03222-3

28. Li CA, Nan J, Ye Q, *et al*. Amplifying anti-tumor immune responses via mitochondria-targeting near-infrared photodynamic therapy. *Adv Sci*. 2025;12(33):2505525.

doi: 10.1002/advs.202505525

29. Liu LG, Sun YM, Liu ZY, *et al*. Halogenated gallium corroles: DNA interaction and photodynamic antitumor activity. *Inorg Chem*. 2021;60(4):2234-2245.

doi: 10.1021/acs.inorgchem.0c03016

30. Fan J, Ding Z, Cai Y, *et al*. Revolutionizing Bone Regeneration: Vascularized Bone Tissue Engineering with Advanced 3D Printing Technology. *Aggregate*. Published online March 6, 2025.

doi: 10.1002/agt2.731

31. Nompumelelo Simelane NW, Kruger CA, Abrahamse H. Photodynamic diagnosis and photodynamic therapy of colorectal cancer in vitro and in vivo. *RSC Adv*. 2020;10(68):41560-41576.

doi: 10.1039/d0ra08617g

32. Mesquita MQ, Dias CJ, Neves MGPM, Almeida A, Faustino MAF. Revisiting Current Photoactive Materials for Antimicrobial Photodynamic Therapy. *Molecules*. 2018;23(10):2424.

doi: 10.3390/molecules23102424

33. Wang H, Ewetse MP, Ma C, *et al*. The "light knife" for gastric cancer: photodynamic therapy. *Pharmaceutics*. 2022;15(1):101.

doi: 10.3390/pharmaceutics15010101

34. Korbelik M. Photodynamic therapy supported by antitumor lipids. *Pharmaceutics*. 2023;15(12):2723.

doi: 10.3390/pharmaceutics15122723

35. Sun B, Chen Y, Yu H, *et al*. Photodynamic PEG-coated ROS-sensitive prodrug nanoassemblies for core-shell synergistic chemo-photodynamic therapy. *Acta Biomater*. 2019;92:219-228.

doi: 10.1016/j.actbio.2019.05.008

36. Wang GD, Nguyen HT, Chen H, *et al*. X-Ray Induced Photodynamic Therapy: A Combination of Radiotherapy and Photodynamic Therapy. *Theranostics*. 2016;6(13):2295-2305.

doi: 10.7150/thno.16141

37. Wang H, Liu H, Guo Y, *et al*. Photosynthetic microorganisms coupled photodynamic therapy for enhanced antitumor immune effect. *Bioact Mater*. 2022;12:97-106.

doi: 10.1016/j.bioactmat.2021.10.028

38. Wei F, Rees TW, Liao X, Ji L, Chao H. Oxygen self-sufficient photodynamic therapy. *Coord Chem Rev*. 2021;432:213714.

doi: 10.1016/j.ccr.2020.213714

39. Tam LKB, Ng DKP. "Click" for precise photodynamic therapy. *Mater Chem Front*. 2023;7(16):3184-3193.

doi: 10.1039/d3qm00431g

40. Wu C, Li Y, Cheng Z, *et al*. Cell-penetrating riboflavin conjugate for antitumor photodynamic therapy. *Chin Chem Lett*. 2022;33(9):4339-4344.

doi: 10.1016/j.cclet.2022.01.036

41. Yu Y, Wang H, Zhuang Z, *et al*. Self-adaptive photodynamic-to-photothermal switch for smart antitumor photoimmunotherapy. *ACS Nano*. 2024;18(20):13019-13034.

doi: 10.1021/acsnano.4c01600

42. Zheng K, Liu H, Liu X, *et al*. Tumor targeting chemo- and photodynamic therapy packaged in albumin for enhanced anti-tumor efficacy. *Int J Nanomedicine*. 2020;15:151-167.

doi: 10.2147/ijn.S227144

43. Yang Y, Ji C, Zhu ZH, *et al*. Metal–organic frameworks based on fluorogens with aggregation-induced emission for enhanced sonodynamic therapy. *Chem Mater*. 2024;36(10):4955-4966.

doi: 10.1021/acs.chemmater.3c02495

44. Kazimierczak P, Benko A, Palka K, Canal C, Kolodynska D, Przekora A. Novel synthesis method combining a foaming agent with freeze-drying to obtain hybrid highly macroporous bone scaffolds. *J Mater Sci Technol*. 2020;43:52-63.

doi: 10.1016/j.jmst.2020.01.006

45. Yuan X, Zhu W, Yang Z, *et al*. Recent advances in 3D printing of smart scaffolds for bone tissue engineering and regeneration. *Adv Mater*. 2024;36(34):2403641.

doi: 10.1002/adma.202403641

46. Song P, Hu C, Pei X, *et al*. Dual modulation of crystallinity and macro-/microstructures of 3D printed porous titanium implants to enhance stability and osseointegration. *J Mater Chem B*. 2019;7(17):2865-2877.

doi: 10.1039/c9tb00093c

47. Wu K, El Zowalaty AE, Sayin VI, Papagiannakopoulos T. The pleiotropic functions of reactive oxygen species in cancer. *Nat Cancer*. 2024;5(3):384-399.

doi: 10.1038/s43018-024-00738-9

48. Zhong K, Zhang Z, Cheng W, *et al*. Photodynamic O2 economizer encapsulated with DNAzyme for enhancing mitochondrial gene-photodynamic therapy. *Adv Healthc Mater*. 2024;13(5):2302495.

doi: 10.1002/adhm.202302495

49. Chen X, Yong Z, Xiong Y, *et al*. Hydroxyethyl starch conjugates co-assembled nanoparticles promote photodynamic

therapy and antitumor immunity by inhibiting antioxidant systems. *Asian J Pharm Sci*. 2024;19(5):100950.

doi: 10.1016/j.ajps.2024.100950

50. He S, Wang L, Wu D, *et al*. Dual-responsive supramolecular photodynamic nanomedicine with activatable immunomodulation for enhanced antitumor therapy. *Acta Pharm Sin B*. 2024;14(2):765-780.

doi: 10.1016/j.apsb.2023.10.006

51. Li J, Xing Y, Chen X. Intercalating of AIEgens into MoS2 nanosheets to induce crystal phase transform for enhanced photothermal and photodynamic synergetic anti-tumor therapy. *Talanta*. 2024;271:125677.

doi: 10.1016/j.talanta.2024.125677

52. Xie X, Zhang S, Liu M, *et al*. Boosting anti-tumor immunity with boron-based nanosheets via photodynamic-elicited pyroptosis and adjuvant delivery. *J Mater Chem B*. 2025;13(28):8380-8394.

doi: 10.1039/d5tb00801h

53. Zhang Y, Ying-Kit C, NDKP, Wing-Ping F. Enhancement of innate and adaptive anti-tumor immunity by serum obtained from vascular photodynamic therapy-cured BALB/c mouse. *Cancer Immunol Immunother*. 2021;70(11):3217-3233.

doi: 10.1007/s00262-021-02917-4